Water Resources Research

RESEARCH ARTICLE
10.1029/2025WR041036

Pore-Scale Rock-Typing and Upscaling of Relative Permeability on a Laminated Sandstone Through Minkowski Measures

Han Jiang[1,2], Bowen Shi[1], Chao-Zhong Qin[1,2], Christoph Arns[3], and S. Majid Hassanizadeh[4]

[1]School of Resources and Safety Engineering, Chongqing University, Chongqing, China, [2]State Key Laboratory of Coal Mine Disaster Dynamics and Control, Chongqing University, Chongqing, China, [3]School of Minerals and Energy Resources, University of New South Wales, Sydney, NSW, Australia, [4]Department of Earth Sciences, University of Utrecht, Utrecht, Netherlands

Abstract Understanding two-phase flow in laminated sandstones is important for fluid migration control and operational strategy determination in underground energy and hydrology engineering projects. Digital core analysis provides unparalleled understanding of two-phase flow in complex porous media, but the integration into field analytical workflow is obstructed by the huge computational burden and imaging limitations on a standard rock core. To address this challenge, we propose a novel pore-scale rock-typing and upscaling approach for fast computation of two-phase flow properties on large three-dimensional digital rock images that contain billions of voxels. Firstly, a heterogeneous rock sample is divided into several homogeneous rock types through data clustering of regional 3D morphological parameters, and their two-phase flow properties are calculated from selected subsamples using in-house pore-network model. The capillary pressure and relative permeability curves of the full digital image are then estimated through quasi-static modeling on the rock type distribution. The excellent agreement between the upscaling results and pore-scale simulations on the full image has verified the effectiveness of this two-phase flow upscaling strategy. With largely reduced computational demands and clearly defined lamination heterogeneity, this approach has demonstrated good potential in bridging the gap between pore-scale and core-scale fluid flow mechanisms. In addition, due to the laminated structural characteristics, we also find a significant reduction in phase mobility over a range of saturations in the relative permeability curves of this highly permeable rock sample.

Plain Language Summary Two-phase flow properties of laminated sandstones are key indexes for production evaluation and optimization throughout the complete underground engineering process. Digital core analysis is a robust tool to study two-phase flow in porous media. Nevertheless, its field application remains underdeveloped because of the infeasibility of core-scale simulations. A key challenge is the massive computational burden from direct numerical simulation on digital rock images of billions of voxels. Therefore, an integrated pore-scale rock type classification and upscaling approach is developed in this work. The results have shown excellent agreement between upscaling and direct computation. This has also demonstrated the potential in inter-resolution applications, which will ultimately facilitate efficient core-scale multi-phase flow computations.

Key Points:

- Regional 3D morphological features on the porous structure of a laminated sandstone are efficiently extracted and utilized for rock-typing
- Two-phase flow properties from the proposed upscaling workflow agree closely with pore-scale simulation results on a full 3D scanning image
- An immobile zone from the relative permeability curves of the highly permeable sandstone is observed due to the laminated structure

Supporting Information:

Supporting Information may be found in the online version of this article.

Correspondence to:

C.-Z. Qin,
chaozhong.qin@cqu.edu.cn

Citation:

Jiang, H., Shi, B., Qin, C.-Z., Arns, C., & Hassanizadeh, S. M. (2026). Pore-scale rock-typing and upscaling of relative permeability on a laminated sandstone through Minkowski measures. *Water Resources Research*, *62*, e2025WR041036. https://doi.org/10.1029/2025WR041036

Received 13 MAY 2025
Accepted 4 DEC 2025

Author Contributions:

Conceptualization: Han Jiang, Chao-Zhong Qin, Christoph Arns
Data curation: Bowen Shi, S. Majid Hassanizadeh
Formal analysis: Han Jiang, Bowen Shi, Chao-Zhong Qin, S. Majid Hassanizadeh
Funding acquisition: Han Jiang, Chao-Zhong Qin, Christoph Arns
Methodology: Han Jiang, Bowen Shi, Chao-Zhong Qin, Christoph Arns, S. Majid Hassanizadeh
Resources: Han Jiang, Christoph Arns
Software: Bowen Shi, Christoph Arns
Supervision: S. Majid Hassanizadeh

1. Introduction

Laminated sandstone is a typical geological formation widespread across the world in oil and gas reservoirs (Karpyn et al., 2009; Lin et al., 2021; Ringrose et al., 1993), aquifers (Masoud & Aldosari, 2020; Swanson et al., 2006) and carbon storage fields (Hayek et al., 2009; Jackson & Krevor, 2020; Li et al., 2024). Its two-phase flow parameters, including capillary pressure and relative permeability curves, are key properties for fluid migration control and the optimization of field operational strategy.

However, the well-developed layering or cross-bedding structure down to millimeter or even smaller scale has strongly aggravated the anisotropy and heterogeneity of the rock samples, and poses a great challenge for accurate prediction of the two-phase flow parameters. Due to excellent operational and economic efficiency, digital rock physics is extensively used to understand the flow mechanisms from pore level (Blunt et al., 2013; Qin & van Brummelen, 2019; Tokan-Lawal et al., 2015; Zhao et al., 2018). To obtain effective flow properties, the

Writing – original draft: Han Jiang, Bowen Shi
Writing – review & editing: Han Jiang, Chao-Zhong Qin, Christoph Arns, S. Majid Hassanizadeh

simulations need to be conducted through a representative elementary volume (REV) of the sample material (Jackson et al., 2018). Yet for multi-phase flow properties, the determination of REV could be very difficult (Armstrong et al., 2014), especially on structures with well-developed laminae (mm) or bedding (cm) (Corbett et al., 1992). Accurate estimation of multi-phase flow properties on such a laminated sample requires thorough investigation on each lamination, which can hardly be achieved by contemporary simulational approaches due to the massive computational burden (Liu et al., 2023) and the trade-off between image resolution and Field of View (FOV) (Botha & Sheppard, 2016).

To reduce the computational burden of full-scale numerical simulation, the idea of pore-scale rock-typing and upscaling workflow has been proposed (Ismail et al., 2013; Ruspini et al., 2021). This homogenization and upscaling framework can be realized through three steps (Ruspini et al., 2021): (a) classify the pore-scale rock structure into different rock types, where each rock type is considered relatively homogeneous; (b) estimate physical properties of every rock type through selected subsamples and propagate back into the rock type distribution map; (c) calculate effective properties of the whole sample through continuum-scale model. Through this approach, the 3D layering inside the rock sample can be clearly captured. Each layer will be considered relatively homogeneous, thus allowing physical property estimation from a few representative subsamples. Meanwhile, rock type distribution map can be largely coarsened before the upscaling computation to save computing resources.

However, rock type classification is challenged by massive data points from a full 3D tomogram of up to 2000^3 voxels. For common image-based deep learning methods, the computational cost and memory demand of convolutional data processing on 3D images have heavily restricted manageable image size and window size. Therefore, application on a full-scale scanning image of billions of voxels is currently impractical. In contrast, we have developed an efficient rock type classification method using the Minkowski functionals (Minkowski measures in regional computations) as the feature descriptors, which are frequently used to characterize structure for the strong correlation with physical properties (Arns et al., 2004, 2009). For the start, regional 3D morphological features of the whole tomogram are computed utilizing integral geometry (Arns et al., 2005). With the unique additivity of the parameters (Mecke, 2000), the huge computational burden brought by the convolutional and voxel-based analytical process is significantly diminished by the introduction of Fast Fourier Transform (FFT) (Jiang & Arns, 2020b). Then, Gaussian Mixture Model (GMM) for data clustering is applied on the Minkowski measures. On this basis, representative two-phase flow properties are determined from simulations on selected subsamples of each rock type. Finally, the capillary pressure and relative permeability curves of the full sample are acquired through quasi-static simulations on the rock type distribution map.

This integrated pore-scale rock-typing and upscaling workflow is applied on a natural laminated sandstone, and the upscaling results of two-phase flow properties have shown an excellent match with pore-scale simulations on the original image. With this proven workflow, the knowledge for lamination recognition can be transferred to low-resolution images of large FOV through supervised classification methods (Jiang & Arns, 2020a). The physical properties of the subsamples can also be utilized for calculations on low-resolution images as well. Given the well-characterized laminal heterogeneity, the feasibility of fluid flow predictions on low-resolution images could be greatly enhanced, thus establishing a solid basis for the upscaling of two-phase flow properties to a standard rock core or even bigger. In addition, we have found an immobile zone from the relative permeability curves of this highly permeable laminated sandstone, which has offered valuable evidence to understand fluid entrapment.

2. Methods and Samples

In this section, we first introduce the laminated sandstone used in the study. Then, the pore-scale rock-typing and upscaling workflow is explained in detail, followed by the methods involved the workflow including the extraction and data clustering of Minkowski measures, the calculation of two-phase flow properties and upscaling of two-phase flow properties on the rock-type map.

2.1. Laminated Sandstone

The rock sample used in this work was collected from the Precipice sandstone of the Surate basin in Australia. The sample is laminated with fine to medium grain layers and contains clay minerals of less than 10%. The digital tomogram is scanned at 5.17 μm/voxel (Figure 1a), and in total 990 × 990 × 3,300 voxels are generated during

10.1029/2025WR041036

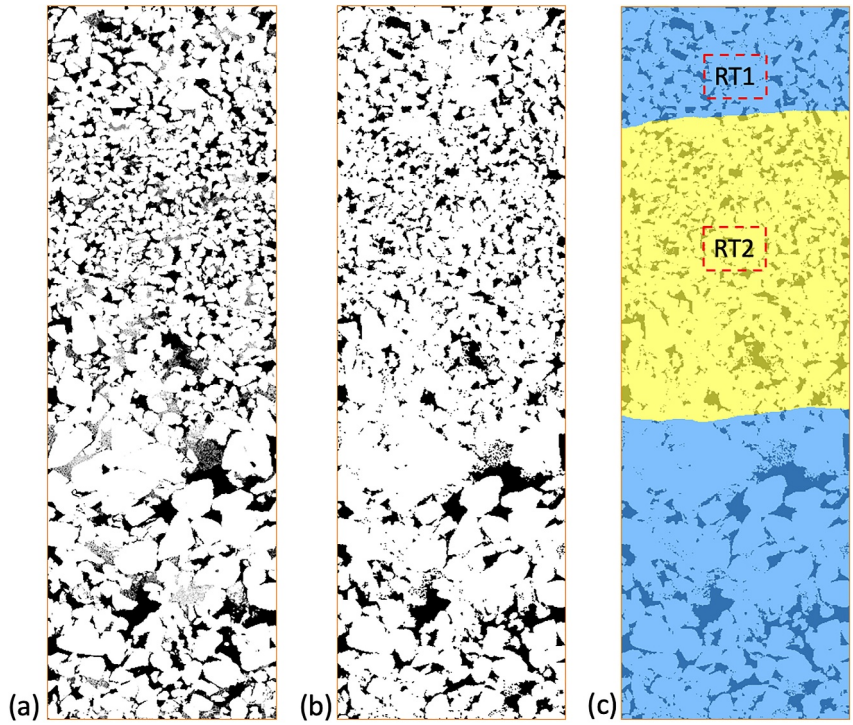

Figure 1. 2D slices of the 3D sandstone image at different stages: (a) grayscale image, (b) segmented image and (c) calculated rock-type field overlapping the segmented image. Bright areas are solid, dark areas are pore space, and gray areas in (a) are clay minerals, which are segmented into solid phase in (b). Blue region in (c) is labeled as rock type 1 (RT1), and yellow region is labeled as rock type 2 (RT2). Image resolution is 5.17 μm/voxel, and the size of the slices is 900 × 2800 voxels.

the scanning process. After getting rid of irregular margins, central 990 × 990 × 3,020 voxels are used in the rock-typing process. Image quality enhancement and phase segmentation are performed using the "mango" image processing software (Xray-CT; morphology; segmentation, 2,004). Here, clay minerals are treated as solid particles, and only resolved pore space is considered to be providing effective fluid flow (Figure 1b). To compute regional Minkowski parameters, the segmented image was scanned by an oblate window of $a = b = 4c$ (a, b and c refer to the half-axes of the window respectively in its three dimensions) and $c = 20, 30, 40, \ldots, 130$. This window size ratio is decided giving the horizontal lamination of the sample. Before the start of the computation, the image was enlarged to offset the shrinkage of the Minkowski fields from regional computations. Both ends of x and y directions are mirrored by the length of a and b.

2.2. Upscaling Workflow

This integrated workflow of pore-scale rock-typing and upscaling of relative permeability is sketched in Figure 2. Firstly, rock type classification on the laminated sandstone is conducted. From the 3D scanning image of the rock sample (Figure 2a), four Minkowski maps (Figure 2b) describing regional structural characteristics of the rock sample are computed. These four measures are comprised of volume, surface area, integral of mean curvature and integral of total curvature. The colors distributed in these maps represent different local measurement values. Then, these maps are input for data clustering using the GMM method and the rock types are classified (Figure 2c). Secondly, representative two-phase flow properties for each rock type are computed. Cubic subsamples for each rock type are selected from the rock-type field, and pore-network modeling is applied to the subsamples for two-phase flow simulation. Figure 2d has presented pore networks extracted from the subsamples, and Figure 2e represents the computed capillary pressure and relative permeability curves of the subsamples. Thirdly, upscaling of two-phase flow properties of the full sample is carried out. Representative two-phase flow properties of each rock type are assigned to the respective computational grids on the rock type field (Figure 2f),

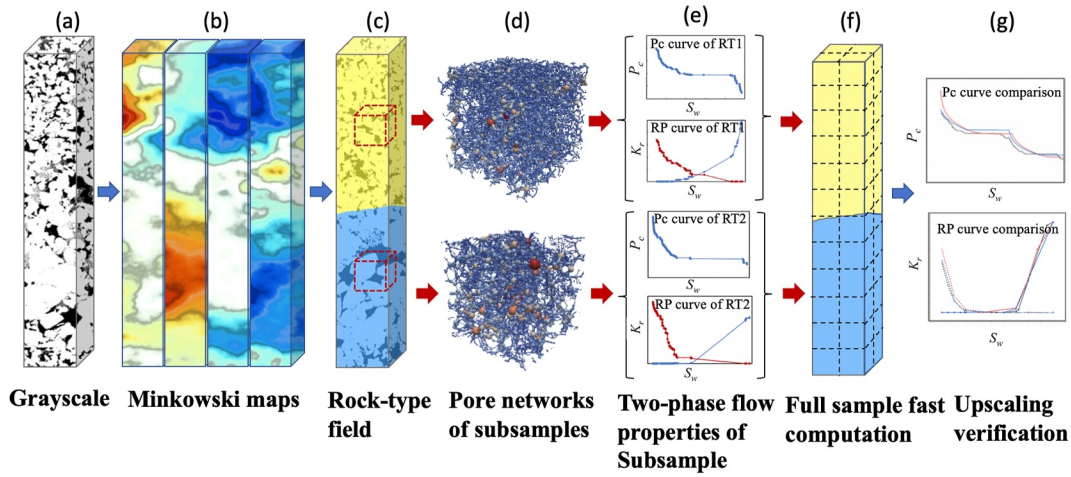

Figure 2. Flow chart of upscaling of two-phase flow properties (RT: rock type, P_c: capillary pressure, RP: relative permeability). (a) Grayscale image of rock sample (black is pore space). (b) Four Minkowski maps computed from the scanning image, including volume, surface area, integral of mean curvature and integral of total curvature. The colors represent different local measurement values. (c) Schematic plot of the rock-type field of the rock sample. Blue and yellow represent different rock types classified from the Minkowski maps. (d) Pore networks of the subsamples of each rock type. (e) Schematic plots of the capillary pressure and relative permeability curves of the subsamples. (f) Schematic plot of the computational grids in the rock-type field. (g) The comparison of two-phase flow properties between upscaling and pore-scale simulation results on the full sample.

in which the computational grids can be largely coarsened from original image voxels to achieve better computational efficiency. Then, two-phase flow simulation on the rock-type field is conducted for capillary pressure and relative permeability curves of the full sample. To verify the upscaling results, pore-scale simulation of two-phase flow properties on the full sample is also conducted, and the results are compared in Figure 2g.

2.3. Pore-Scale Rock Type Classification Using Minkowski Measures

To obtain the rock type classification results, we first extract local spatial features of the porous sample. In this study, we use a set of robust descriptive parameters called Minkowski functionals, which are comprised of volume $V(Y)$, surface area $S(Y)$, integral of mean curvature $M(Y)$ and integral of total curvature $K(Y)$. The definition of Minkowski functionals over a regional window has been previously described in (Arns et al., 2005; Jiang & Arns, 2020b). For a body Y with a sufficiently smooth surface ∂Y in $\mathbb{R}^3$, these parameters are defined as:

$$\begin{aligned} S(Y) &= \int_{\partial Y} ds, \\ M(Y) &= \int_{\partial Y} \frac{1}{2}\left(\frac{1}{r_1(s)} + \frac{1}{r_2(s)}\right) ds, \\ K(Y) &= \int_{\partial Y} \frac{1}{r_1(s)\, r_2(s)}\, ds. \end{aligned} \tag{1}$$

in which $r_1(s)$ and $r_2(s)$ are the maximum and minimum curvature radii at location s of Y, respectively.

To obtain Minkowski measures from digital images which is made of discretized cubic voxels, the intrinsic volumes are related for the interpretation of the sample structure (Arns et al., 2009):

$$
\begin{aligned}
V_0(Y) &= \frac{1}{4\pi}K(Y) = \chi(Y),\\
V_1(Y) &= \frac{1}{3\pi}M(Y),\\
V_2(Y) &= \frac{1}{6}S(Y),\\
V_3(Y) &= V(Y).
\end{aligned}
\tag{2}
$$

Here, the intrinsic volumes are regulated to be $V_0 = V_1 = V_2 = V_3 = 1$ for one voxel.

To extract the maps of regional Minkowski measures, a sliding window is arranged to scan through the segmented tomogram of the rock sample consecutively by three dimensions, in which the voxels are filled with either solid or pore space. For a regional structure inside the sliding window, the process starts with a minimum cubic unit of 2^3 voxels, and the corresponding intrinsic volumes of each possible spatial combination of solid or void phase in this cubic unit are calculated. Considering the rotational symmetry of the cubic unit, 22 spatial combinations can be found for binary images. Detailed information of the spatial combinations and their corresponding intrinsic volumes can be found in (Jiang & Arns, 2020b). To obtain regional Minkowski measures in a sliding window, each cubic unit of 2^3 voxels comprising the regional structure will be assigned its intrinsic volumes according to its spatial relationship (one of the 22 possibilities). Then, the resulting histogram of intrinsic volumes can be directly summed up and converted into Minkowski measures, which is facilitated by the additivity of Minkowski functionals due to the involvement of integral geometry as indicated in Equation 1. For every location of the sliding window in the tomogram, we will need to compute its regional Minkowski measures in this manner to obtain the 3D Minkowski maps of the full image. However, the computation of these parameters on the full image would require an enormous number of arithmetic operations and computational resources that can hardly be achieved on personal workstations. To accelerate this process and alleviate the computational burden, FFT is introduced into the process as allowed by the additivity of Minkowski functionals (Jiang & Arns, 2020b).

Instead of direct summation of the intrinsic volumes of all possible 2^3-voxel cubic units in every window as in previous works (Ismail et al., 2013), these 22 types of spatial combinations will be processed through FFT convolution separately. Firstly, the intrinsic volumes of every possible 2^3-voxel cubic units in the whole image are determined. Next, the distributions of each spatial combination are extracted separately. Then, the resulting 22 distributions are calculated through FFT convolution using the same window size before they are summed up. With the help of FFT convolution, the exponential growth of arithmetic operations brought by a regional window can be alleviated, which is especially convenient for the application on natural samples as a big window size is normally needed (Jiang & Arns, 2020a). More details about the involvement of FFT can be found in (Jiang & Arns, 2020b). The classification of the feature data set is accomplished utilizing an unsupervised clustering method called multi-variate Gaussian mixture model (Jiang & Arns, 2020b; Ribeiro, 2004) which considers all four Minkowski measures. By labeling all the data points according to the classification results, we obtain the spatial distribution of different rock types in the tomogram.

2.4. Computing Relative Permeability of Subsamples From the Pore-Scale

The computation of relative permeability and capillary pressure curves is realized using in-house pore-network model (Shi et al., 2024). Comparing with other numerical simulation approaches such as Lattice Boltzmann or finite volume method, pore-network models excel at computational efficiency, and has been verified by experimental measurements of its computational reliability (Dong & Blunt, 2009; Valvatne & Blunt, 2004). As full image two-phase flow simulations are needed for the verification of the upscaling workflow, which has $990 \times 990 \times 3{,}020$ voxels, pore-network modeling is preferred in this study. To extract the pore networks, a robust pore-network generator called PoreSpy is applied on the segmented tomogram to obtain pore locations, inscribed and extended radii, and the connectivity map of pore bodies (Gostick, 2017). After measuring the shape factors of pore bodies and throats, they will be represented by simplified pore elements of capillary tubes. The cross-section of the tubes can be circular, triangular or square according to the shape factors. The capillary pressure and relative permeability curves are simulated under quasi-static conditions. Detailed information of the simulation process can be found in Text S2 in Supporting Information S1.

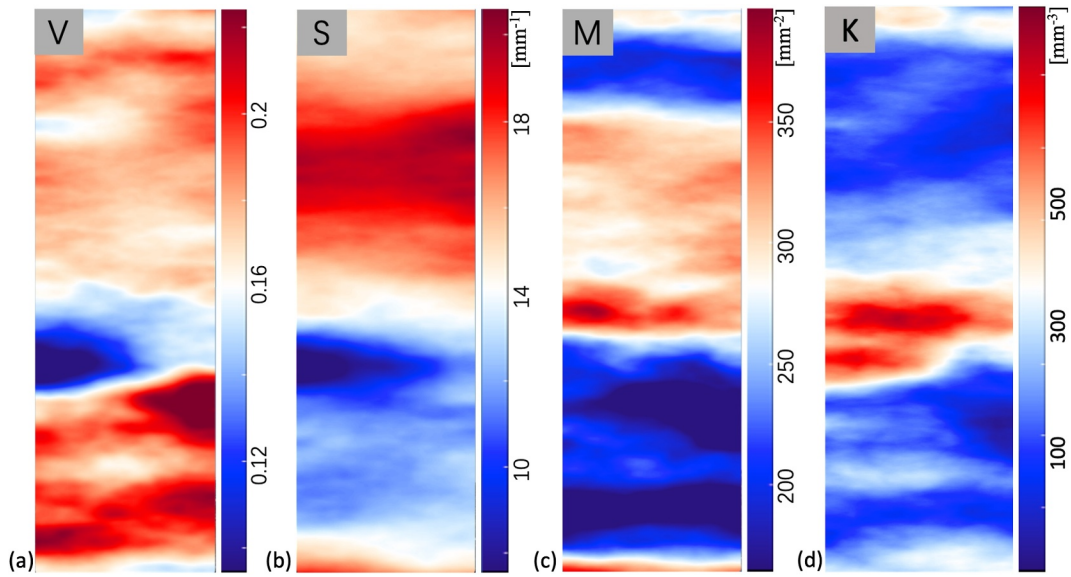

Figure 3. X–Z slices of 3D Minkowski maps of laminated sandstone computed from regional window size of $a = b = 4c, c = 110$ voxels. (a–d) are 2D slices of volume (V), surface area (S), integral of mean curvature (M) and integral of total curvature (K), respectively.

2.5. Computing Relative Permeability of the Full Sample Through the Rock-Type Field

After rock type classification on the full scanning image, representative subsample for each rock type is selected for the calculation of capillary pressure and relative permeability curves. Then, the curves are fit into the van Genuchten model (Van Genuchten, 1980), which offers a continuous relationship between pressure and hydraulic parameters for follow-up steps. These properties estimated from representative subsamples are assigned to the areas of their respective rock type in return. Under a given invading pressure, the saturation and hydraulic conductance values for each computational grid can be determined from the fitted models. On the basis of the volumetric conservation equation, these values are used in the construction of a linear equation system for the solution of pressure distribution over the whole image, then the flow rate and relative permeability of the full sample are estimated. Repeating this computational workflow through the drainage and imbibition process, relative permeability and capillary pressure curves of the full sample can be obtained. More details about the upscaling workflow can be found in Text S2 in Supporting Information S1. To verify the upscaling results, pore-scale computation on the original structure of the full image has been carried out following the method introduced in Section 2.4.

3. Results

3.1. Rock Type Classification

Given the distribution of grain size on different laminations, a regional window of $a = b = 4c, c = 110$ voxels was used to compute the Minkowski measures, and the 2D slices of regional Minkowski measures are shown in Figure 3. The determination of window size have a significant influence on the classification results when using unsupervised classification method like GMM. For samples with strongly heterogeneous particle size distribution, it may require tests on multiple sizes. One can also choose supervised classification models such as support vector machines, through which the sensitivity on window size can be largely reduced with a small amount of manually labeled data (Jiang et al., 2024).

We assigned two rock types for classifying this sample. The classification result is presented in Figure 1c, in which the blue region is labeled as Rock Type (RT) 1, and the yellow region is labeled as rock type 2. It can be seen from Figure 1c that the two types have distinctive structural characteristics from each other and are quite homogeneous within the same type. Detail operational information about the classification process can be found in Text S1 in Supporting Information S1. To verify the classification results, we computed single-phase

Table 1
Average Permeabilities and Porosities of the Rock Types

	k_h	k_v	ϕ
RT1	7.764 ± 1.630	6.176 ± 2.311	0.181 ± 0.014
RT2	1.000 ± 0.107	0.729 ± 0.093	0.165 ± 0.007

permeability of the full image from the rock type map and compared it with pore-scale computational results from the original image. Firstly, 13 subsamples of 500^3 voxels were picked up for both rock types to compute average permeability values. The average permeability and porosity of the rock types are listed in Table 1. The porosities of both rock types are very similar, while permeabilities are quite distinctive from each other. Then, the average permeability values are assigned to every data point in the region of the respective rock type as hydraulic conductance values for fast full image computation using Darcy's law through the rock type distribution. Other details about permeability upscaling can also be found in (Jiang et al., 2024). The comparison between the upscaling and direct computation results is given in Table 2. We can see that the accuracy of upscaling results is over 94%, which has proved the effectiveness of the rock type classification results and illustrated the potential of the workflow for application on a wider scale and two-phase flow properties.

3.2. Upscaling of Relative Permeability

For the upscaling of two-phase flow properties from the rock-type field, the properties of each rock type need to be collected. In this work, we simulated the two-phase flow process using in-house pore-network model. The extracted pore-network models from the subsamples of both rock types are presented in Figure 4. The upper pore-network model from RT2 has smaller pore bodies with a higher density distribution, while the lower pore-network model from RT1 has larger pore bodies but a sparser distribution. For RT1, 65 subsamples of 500^3 voxels can be extracted with an interval of 100 voxels, while 125 subsamples can be extracted for RT2. For thinly laminated structure, available subsample size from the rock types may be smaller than a REV, especially when it comes to two-phase flow. To ensure the accuracy of the upscaling process, the fluctuation of flow parameters from this subsample size is recorded through the variety of subsamples and assigned to the computational grids using random assignment or averaged values. The drainage-imbibition process is simulated for each subsample using the intrusion percolation algorithm, and comparative 3D illustrations of fluid distribution in the subsamples from different rock types during the simulation process are given in Figure 5. The scatter plots of relative permeability and capillary pressure curves are obtained from the simulations and are shown in Figure 6. Figure 6a presents the scatter plots of capillary pressure curves from 20 subsamples of RT1. We can observe good similarity between the curves, suggesting homogeneity of the porous structure within the rock type. As the pressure increases to around 20 kPa, water saturation drops dramatically from 0.9 to 0.3, indicating a relatively uniform distribution of pore size in RT1. Scatter plots of capillary pressure curves of RT2 (Figure 6b) have similar characteristics, but with much higher intrusion pressure and slower saturation reduction, indicating smaller average pore throat sizes with sparser distribution as shown in Figure 4. Scatter plots of relative permeability curves are given in Figures 6c and 6d. Curves of the same rock type have presented a similar trend, providing further evidence of the validity of the rock type classification.

With representative two-phase flow properties from the subsamples, the relative permeability and capillary pressure curves of the full sample can be efficiently computed from the rock type distribution map. The results from pore-scale simulations on the original image and upscaling computations of different data assigning schemes are compared in Figure 7. The two-phase flow properties from the subsamples can be randomly assigned to the data points to keep the rock type's mild heterogeneity (random assignment method), or the whole rock type can be assigned by the averaged results of the subsamples (average method). The data from all the subsamples of 500^3 voxels are used for the above two methods ("hetall" and "homall" in Figure 7). Meanwhile, 10 subsamples for each rock type have been selected for the same task ("het10" and "hom10" in Figure 7). Figure 7c demonstrates the capillary pressure curves of the full sample from the drainage and imbibition simulations. The black curve is generated from pore-scale simulations on the original segmented tomogram using PNM, and the colored curves are generated from the upscaling method. All results from the upscaling workflow have successfully captured the stepped feature of the drainage curve from PNM computation and followed the slow and small increase of WP saturation on the imbibition curve. The utilization of 10 subsamples can already produce very good match with the PNM results, guaranteeing great efficiency for the computation of representative properties of each rock type. In Figures 7a and 7b, relative permeability curves computed from the

Table 2
Full Image Permeabilities From Direct and Upscaling Computation

Scenario	k_h	k_v
Direct computation	4.40	1.47
Upscaling computation	4.65(+5.68%)	1.45(−1.36%)

10.1029/2025WR041036

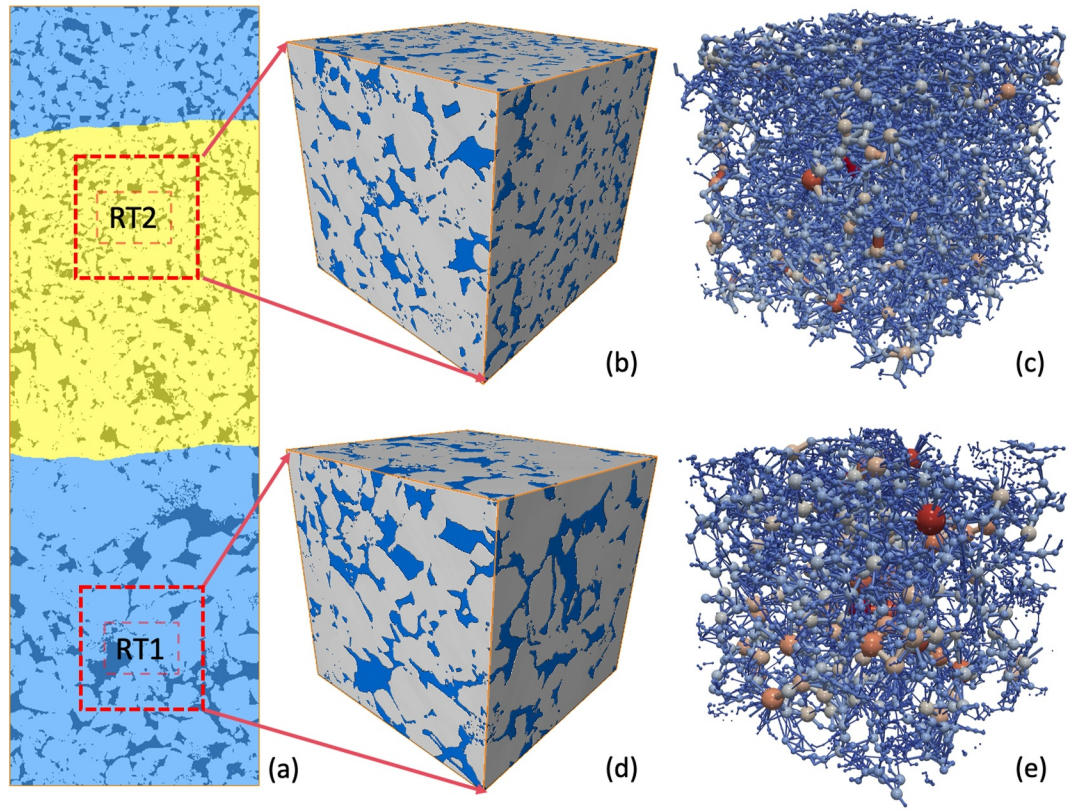

Figure 4. Illustration of the pore-network models of subsamples from each rock type. (a) 2D slice of the rock-type field on top of the segmented image of the sandstone, (b) 3D illustration of the porous structure of a subsample from rock type 2, (c) the generated pore network from (b), (d) 3D illustration of the porous structure of a subsample from rock type 1, (e) the generated pore network from (d).

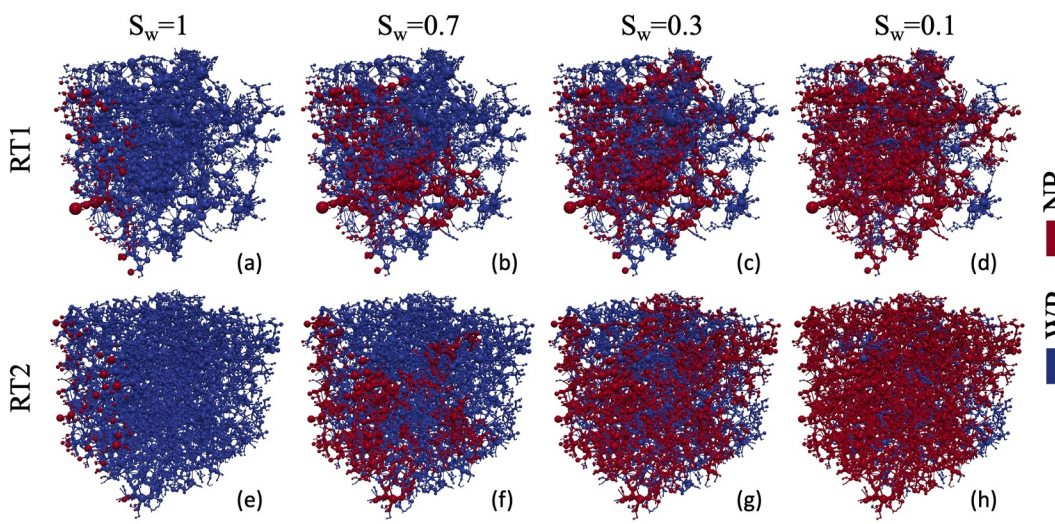

Figure 5. 3D illustrations of the drainage process of subsamples from each rock type. (a–d) Different intrusion stages on a subsample from RT1; (e–h) Different intrusion stages on a subsample from RT2. WP refers to the wetting phase, and NP refers to the non-wetting phase. S_w measures the saturation of the wetting phase.

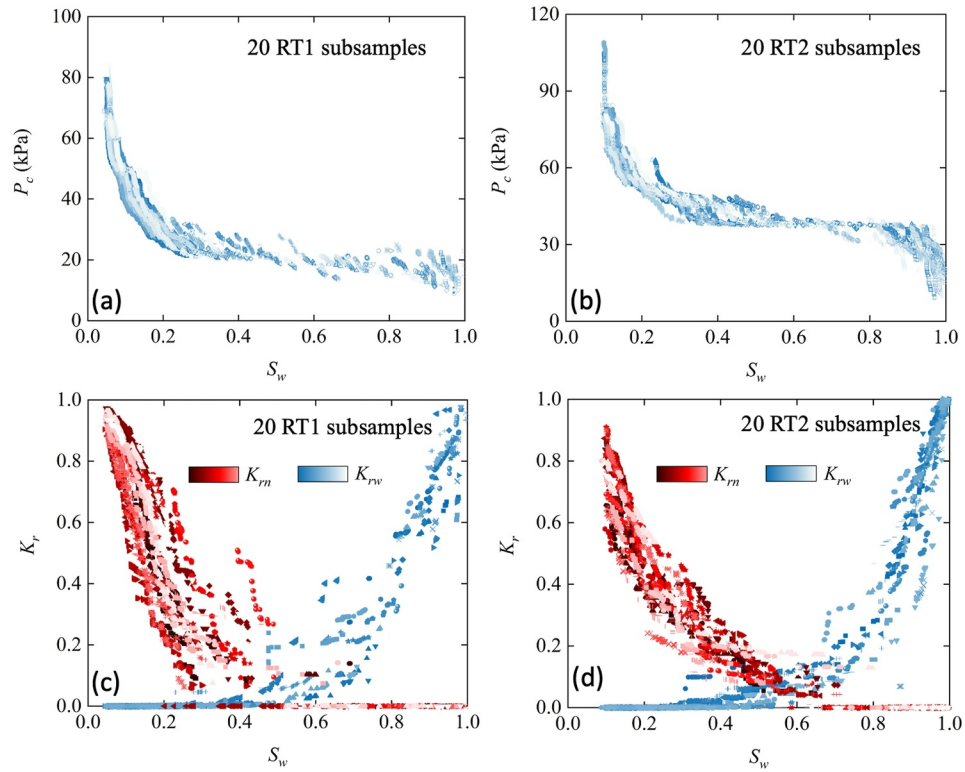

Figure 6. Scattered plots of capillary pressure and relative permeability curves for each rock type during the drainage process: (a–b) capillary pressure curves of 20 subsamples from RT1 and RT2, (c–d) relative permeability curves of 20 subsamples from RT1 and RT2. K_{rw} represents the relative permeability of the wetting phase, and K_{rw} is the relative permeability of the non-wetting phase.

drainage and imbibition simulations are presented. The data points from upscaling computations closely overlap the PNM results, among which "hom10" has slightly outperformed the others. The deviation of upscaling results from random assignment method may be caused by inadequate subsample numbers. Considering the demand in subsamples and upscaling performance, average method is more recommended for the upscaling workflow. However, when it comes to special cases of strongly heterogeneous layers, random assignment method is more suitable for maintaining heterogeneity information.

Although we may need to test on more complicated and larger rock samples, the results have demonstrated the feasibility and potential of the proposed workflow. Regarding the computational efficiency of the upscaling method, the computational grids needed in the upscaling computation can be restricted to thousands with carefully preserved boundaries of rock types utilizing convolutional grid coarsening method (Shi et al., 2024). Comparing with pore-scale computation of the full sample using pore-network model, which has approximately 100,000 computational units, the computational resources and computing time required by the upscaling method are largely reduced. Hence, this upscaling method is very promising for bridging the gap between pore-scale and core-scale multiphase flow and building up close interaction between digital physical analysis and laboratory or even field data. Moreover, with the coarsened rock type distribution map, it would be convenient to study dynamic flow problems such as preferential flow, in which the computational improvement would be increasingly evident.

4. Discussion

Given the laminated structure of the rock sample, it is reasonable to hypothesize that the two-phase flow properties are strongly anisotropic. In this study, we focus on one scenario of vertical drainage from the bottom to the top of the sample for a better understanding of the impact of laminations. From the relative permeability curves of the drainage process, we can observe an immobile zone from $S_w = 0.4$ to 0.65 where both NP and WP's

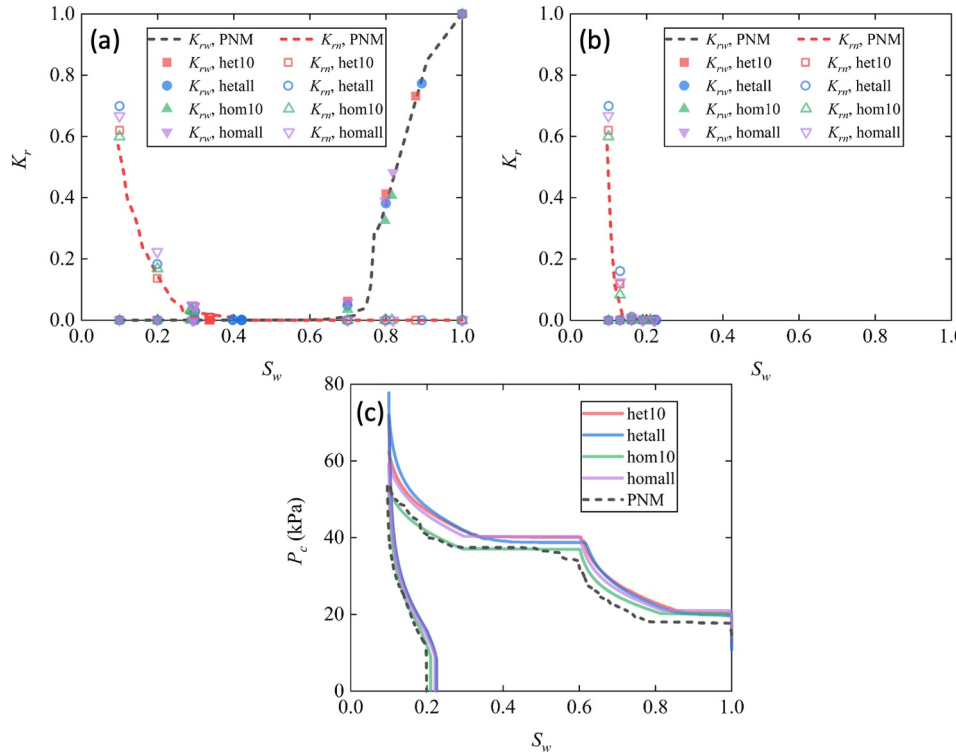

Figure 7. Capillary pressure and relative permeability curves of the full sample: (a) relative permeability curves from the drainage process; (b) relative permeability curves from the imbibition process; (c) capillary pressure curves from direct PNM computation and different upscaling workflows (het10: the properties from 10 subsamples of 500^3 voxels are randomly assigned to the data points of the respective rock type; hetall: the properties from all possible subsamples of 500^3 voxels are randomly assigned to the data points of the respective rock type; hom10: the averaged properties from 10 subsamples of 500^3 voxels are uniformly assigned to all the data points of the respective rock type; homall: the averaged properties from all possible subsamples of 500^3 voxels are uniformly assigned to all the data points of the respective rock type).

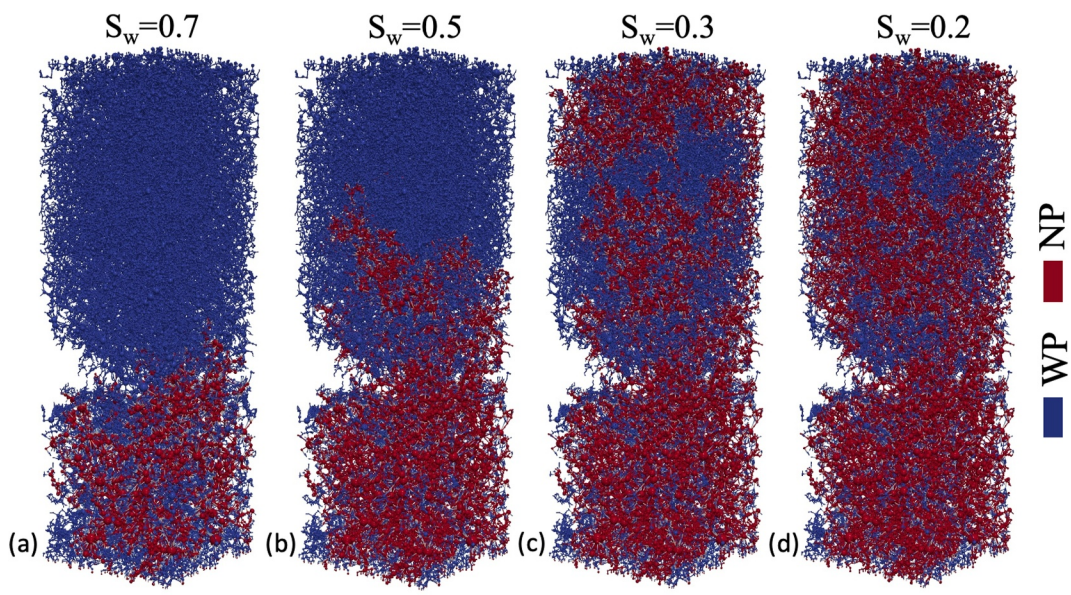

Figure 8. Pore networks of the full image at different drainage stages. The non-wetting phase is drained vertically from the bottom to the top of the sample. The blue regions are filled by the wetting phase, and the red regions are filled by the non-wetting phase. S_w measures the saturation of the wetting phase.

permeabilities are zero. The pore networks of the full image from this drainage process are plotted in Figure 8, through which the spatial distribution of the fluids inside the rock sample is explicitly presented. The blue regions are occupied by NP while the red regions are occupied by WP. From Figure 8a, we can see that NP is stuck at the lower RT1 section. This is because the entry pressure of RT2 is much higher as the passages narrow down, which can also be predicted from the permeability difference in Table 1 where the permeability of RT2 is about 10 times smaller than RT1. Therefore, NP is stranded and gradually replaces WP from big pores to small pores, leading to a fast and dramatic decrease of WP mobility. As the invading pressure increases, NP slowly squeezes into RT2 (Figure 8b). Once a connected pathway is established in RT2 as the invading pressure reaches the breakthrough point, NP will be drained to the upper RT1 region (Figure 8c). Although NP has occupied a large portion of the pore space, its mobility is held back by the limited paths in RT2. As the invading pressure continues to increase, more paths are established for NP in RT2 (Figure 8d), finally improving the permeability of NP as shown in Figure 7a.

After the invading pressure of primary drainage process reaches the preset maximum value, the pressure starts to reduce to allow main imbibition. As WP is imbibed, the WP film attached to the solid grows thicker and merges firstly at narrow throats, which traps NP in pore bodies. This entrapment is much more severe in RT2 of smaller pore and throat size, and has blocked the fluid movement of the whole sample. Hence, the relative permeability of the secondary imbibition process drops rapidly to 0 as shown in Figure 7b, and the increase of WP saturation in the imbibition process is limited (Figure 7c) as well.

In fact, both RT1 and RT2 have very good intrinsic permeabilities, but this relatively small difference, coupled with the laminated structure, has caused heavy fluid blockage in multi-phase flow, creating an immobile zone in the relative permeability curves. In engineering practices such as hydrocarbon depletion, this is going to heavily affect oil and gas recovery. On the other hand, the good match between direct computation and upscaling results suggests that rock type classification using Minkowski functionals is quite effective in recognizing regions of different flow patterns, which can be particularly useful in understanding preferential flows in heterogeneous porous media and ultimately contribute to the enhancement of engineering practices and industrial applications such as material design optimization.

5. Conclusions

Two-phase flow in porous media is an important physical process and frequently occurs in many industrial and underground energy projects. Digital physical analysis integrating advanced microscopic imaging offers a powerful research tool to understand the fundamentals of two-phase flow. However, current research scale is strictly limited by the heavy computational burden of the simulational process, and can hardly be merged to field analytical workflow considering the strong heterogeneity of rock structures. Toward this problem, an integrated pore-scale rock-typing and upscaling workflow is proposed and has achieved fast computation of relative permeability on a full 3D image of billions of voxels. In this workflow, Minkowski functionals are chosen to describe regional morphological and topological characteristics of the porous structure. Fast Fourier transform is introduced to accelerate the convolutional process for the generation of regional Minkowski maps. Then, the regional maps are utilized for rock type recognition through multi-variant Gaussian mixture model. When pore-scale rock-typing is accomplished, representative two-phase flow properties are computed for each rock type from limited subsamples and used for the fast computation of relative permeability from the rock type distribution map of the full image. The main conclusions are listed as follows:

1. Pore-scale rock-typing using Minkowski functionals enables automatic classification of different lamination.
2. Effective permeability of the full scanning image computed from upscaling workflow has reach the accuracy of 95% comparing with pore-scale computational results.
3. Upscaling of relative permeability from the rock type classification map agrees very well with the results from PNM computation on the full image, which shows the potential of the pore-scale rock-typing and upscaling workflow in bridging the gap between micro-scale and core-scale multi-phase flow mechanisms.
4. An immobile zone has occurred on the relative permeability curves of the full image. The lamination of a relatively less permeable rock type has caused strong fluid blockage and dramatic decrease of the transport ability of the fluids.

Conflict of Interest

The authors declare no conflicts of interest relevant to this study.

Data Availability Statement

The images and permeability data of this article are available at (Jiang et al., 2025). The in-house PNM for relative permeability computation can be found in (Shi et al., 2024).

Acknowledgments
HJ acknowledges the support of National Natural Science Foundation of China (No. 42404136 and No. U23A20595) and the Fundamental Research Funds for the Central Universities (No. 2024CDJXY025). CZQ and MH acknowledge the support of the National Foreign Experts Project (No. S20240032). CHA acknowledges the support of the Australian Research Council for funding through ARC discovery projects DP160104995 and DP200103548.

References

Armstrong, R. T., Georgiadis, A., Ott, H., Klemin, D., & Berg, S. (2014). Critical capillary number: Desaturation studied with fast x-ray computed microtomography. *Geophysical Research Letters*, *41*(1), 55–60. https://doi.org/10.1002/2013gl058075

Arns, C. H., Knackstedt, M. A., & Mecke, K. R. (2004). Characterisation of irregular spatial structures by parallel sets and integral geometric measures. *Colloids and Surfaces A: Physicochemical and Engineering Aspects*, *241*(1–3), 351–372. https://doi.org/10.1016/j.colsurfa.2004.04.034

Arns, C. H., Knackstedt, M. A., & Mecke, K. R. (2009). Boolean reconstructions of complex materials: Integral geometric approach. *Physical Review E*, *80*(5), 051303. https://doi.org/10.1103/physreve.80.051303

Arns, C. H., Mecke, J., Mecke, K. R., & Stoyan, D. (2005). Second-order analysis by variograms for curvature measures of two-phase structures. *European Physical Journal B: Condensed Matter and Complex Systems*, *47*(3), 397–409. https://doi.org/10.1140/epjb/e2005-00338-5

Blunt, M. J., Bijeljic, B., Dong, H., Gharbi, O., Iglauer, S., Mostaghimi, P., et al. (2013). Pore-scale imaging and modelling. *Advances in Water Resources*, *51*, 197–216. https://doi.org/10.1016/j.advwatres.2012.03.003

Botha, P. W., & Sheppard, A. P. (2016). Mapping permeability in low-resolution micro-CT images: A multiscale statistical approach. *Water Resources Research*, *52*(6), 4377–4398. https://doi.org/10.1002/2015wr018454

Corbett, P., Ringrose, P., Jensen, J., & Sorbie, K. (1992). Laminated clastic reservoirs: The interplay of capillary pressure and sedimentary architecture. In *Spe annual technical conference and exhibition?* (pp. SPE–24699).

Dong, H., & Blunt, M. J. (2009). Pore-network extraction from micro-computerized-tomography images. *Physical Review E: Statistical, Nonlinear, and Soft Matter Physics*, *80*(3), 036307. https://doi.org/10.1103/physreve.80.036307

Gostick, J. T. (2017). Versatile and efficient pore network extraction method using marker-based watershed segmentation. *Physical Review E*, *96*(2), 023307. https://doi.org/10.1103/physreve.96.023307

Hayek, M., Mouche, E., & Mügler, C. (2009). Modeling vertical stratification of co2 injected into a deep layered aquifer. *Advances in Water Resources*, *32*(3), 450–462. https://doi.org/10.1016/j.advwatres.2008.12.009

Ismail, N. I., Latham, S., & Arns, C. H. (2013). Rock-typing using the complete set of additive morphological descriptors. In *Spe reservoir characterisation and simulation conference and exhibition* (pp. SPE–165989).

Jackson, S. J., Agada, S., Reynolds, C. A., & Krevor, S. (2018). Characterizing drainage multiphase flow in heterogeneous sandstones. *Water Resources Research*, *54*(4), 3139–3161. https://doi.org/10.1029/2017wr022282

Jackson, S. J., & Krevor, S. (2020). Small-scale capillary heterogeneity linked to rapid plume migration during co 2 storage. *Geophysical Research Letters*, *47*(18), e2020GL088616. https://doi.org/10.1029/2020gl088616

Jiang, H., & Arns, C. (2020a). A pore-scale upscaling approach for laminated sandstones using minkowski maps and hydraulic attributes. *Water Resources Research*, *56*(8), e2020WR027978. https://doi.org/10.1029/2020wr027978

Jiang, H., Arns, C., Yuan, Y., & Qin, C.-Z. (2024). Svm-based fast 3d pore-scale rock-typing and permeability upscaling for complex rocks using minkowski functionals. *Advances in Water Resources*, *183*, 104605. https://doi.org/10.1016/j.advwatres.2023.104605

Jiang, H., & Arns, C. H. (2020b). Fast fourier transforms and support-shift techniques for pore-scale microstructure classification using additive morphological measures. *Physical Review E*, *101*(3), 033302. https://doi.org/10.1103/physreve.101.033302

Jiang, H., Shi, B., Qin, C.-Z., Arns, C., & Hassanizadeh, M. (2025). Pore-scale rock-typing and upscaling of relative permeability on a laminated sandstone through minkowski measures [Dataset]. *Zenodo*. https://doi.org/10.5281/zenodo.15348519

Karpyn, Z., Halleck, P., & Grader, A. (2009). An experimental study of spontaneous imbibition in fractured sandstone with contrasting sedimentary layers. *Journal of Petroleum Science and Engineering*, *67*(1–2), 48–56. https://doi.org/10.1016/j.petrol.2009.02.014

Li, Y., Yang, Y., Dong, M., Imani, G., Yao, J., Zhang, K., et al. (2024). Pore-scale characterization of co2 trapping and oil displacement in three-phase flow in a heterogeneous layered sandstone. *SPE Journal*, *29*(2), 1147–1160. https://doi.org/10.2118/217996-pa

Lin, Q., Bijeljic, B., Raeini, A. Q., Rieke, H., & Blunt, M. J. (2021). Drainage capillary pressure distribution and fluid displacement in a heterogeneous laminated sandstone. *Geophysical Research Letters*, *48*(14), e2021GL093604. https://doi.org/10.1029/2021gl093604

Liu, M., Ahmad, R., Cai, W., & Mukerji, T. (2023). Hierarchical homogenization with deep-learning-based surrogate model for rapid estimation of effective permeability from digital rocks. *Journal of Geophysical Research: Solid Earth*, *128*(2), e2022JB025378. https://doi.org/10.1029/2022jb025378

Masoud, A. A., & Aldosari, A. A. (2020). Groundwater quality assessment of a multi-layered aquifer in a desert environment: A case study in wadi ad-dawasir, Saudi Arabia. *Water*, *12*(11), 3020. https://doi.org/10.3390/w12113020

Mecke, K. R. (2000). Additivity, convexity, and beyond: Applications of minkowski functionals in statistical physics. In *Statistical physics and spatial statistics: The art of analyzing and modeling spatial structures and pattern formation* (pp. 111–184). Springer.

Qin, C.-Z., & van Brummelen, H. (2019). A dynamic pore-network model for spontaneous imbibition in porous media. *Advances in Water Resources*, *133*, 103420. https://doi.org/10.1016/j.advwatres.2019.103420

Ribeiro, M. I. (2004). *Gaussian probability density functions: Properties and error characterization*. Institute for Systems and Robotics.

Ringrose, P., Sorbie, K., Corbett, P., & Jensen, J. (1993). Immiscible flow behaviour in laminated and cross-bedded sandstones. *Journal of Petroleum Science and Engineering*, *9*(2), 103–124. https://doi.org/10.1016/0920-4105(93)90071-l

Ruspini, L., Øren, P., Berg, S., Masalmeh, S., Bultreys, T., Taberner, C., et al. (2021). Multiscale digital rock analysis for complex rocks. *Transport in Porous Media*, *139*(2), 301–325. https://doi.org/10.1007/s11242-021-01667-2

Shi, B., Jiang, H., Guo, B., Tian, J., & Qin, C.-Z. (2024). Modeling of flow and transport in multiscale digital rocks aided by grid coarsening of microporous domains. *Journal of Hydrology*, *633*, 131003. https://doi.org/10.1016/j.jhydrol.2024.131003

Swanson, S. K., Bahr, J. M., Bradbury, K. R., & Anderson, K. M. (2006). Evidence for preferential flow through sandstone aquifers in southern wisconsin. *Sedimentary Geology*, *184*(3–4), 331–342. https://doi.org/10.1016/j.sedgeo.2005.11.008

Tokan-Lawal, A., Prodanović, M., & Eichhubl, P. (2015). Investigating flow properties of partially cemented fractures in travis peak formation using image-based pore-scale modeling. *Journal of Geophysical Research: Solid Earth*, *120*(8), 5453–5466. https://doi.org/10.1002/2015jb012045

Valvatne, P. H., & Blunt, M. J. (2004). Predictive pore-scale modeling of two-phase flow in mixed wet media. *Water Resources Research*, *40*(7), W07406. https://doi.org/10.1029/2003wr002627

Van Genuchten, M. T. (1980). A closed-form equation for predicting the hydraulic conductivity of unsaturated soils. *Soil Science Society of America Journal*, *44*(5), 892–898. https://doi.org/10.2136/sssaj1980.03615995004400050002x

Zhao, Y., Zhu, G., Zhang, C., Liu, S., Elsworth, D., & Zhang, T. (2018). Pore-scale reconstruction and simulation of non-darcy flow in synthetic porous rocks. *Journal of Geophysical Research: Solid Earth*, *123*(4), 2770–2786. https://doi.org/10.1002/2017jb015296